Biophysical Journal
Article

Biophysical Society

Local Turgor Pressure Reduction via Channel Clustering

Jonah K. Scher-Zagier[1] and Anders E. Carlsson[1,*]
[1]Department of Physics, Washington University, Saint Louis, Missouri

ABSTRACT The primary drivers of yeast endocytosis are actin polymerization and curvature-generating proteins, such as clathrin and BAR domain proteins. Previous work has indicated that these factors may not be capable of generating the forces necessary to overcome turgor pressure. Thus local reduction of the turgor pressure, via localized accumulation or activation of solute channels, might facilitate endocytosis. The possible reduction in turgor pressure was calculated numerically, by solving the diffusion equation through a Legendre polynomial expansion. It was found that for a region of increased permeability having radius 45 nm, as few as 60 channels with a spacing of 10 nm could locally decrease the turgor pressure by 50%. We identified a key dimensionless parameter, $p = P_1 a/D$, where P_1 is the increased permeability, a is the radius of the permeable region, and D is the solute diffusion coefficient. When $p > 0.44$, the turgor pressure is locally reduced by >50%. An approximate analytic theory was used to generate explicit formulas for the turgor pressure reduction in terms of key parameters. These findings may also be relevant to plants, where the mechanisms that allow endocytosis to proceed despite high turgor pressure are largely unknown.

INTRODUCTION

Clathrin-mediated endocytosis (CME) contributes to numerous biological processes, such as cell growth, viral invasion, and neural signaling (1). It involves the inward bending of a portion of the lipid bilayer, which subsequently pinches off to form a vesicle that moves into the cytoplasm. CME has been studied extensively in yeast, due to the ease of genetic manipulation and fluorescent labeling. In yeast, CME involves actin polymerization as well as clathrin and BAR-domain proteins, which help drive invagination through a nonzero preferred curvature. It is believed (2–5) that growing actin filaments exert pushing forces on the membrane, which drive the actin network into the cytoplasm. This motion of the actin network exerts pulling forces to drive invagination, through a coupling via the adaptor protein Sla2. Recent theoretical work on CME in yeast has treated the mechanics of forces generated by actin polymerization, as well as the intrinsic curvature of the clathrin coat that accumulates on the cell membrane (5–8). To date, however, it is not known how actin and other curvature-generating proteins can produce enough force to overcome the large turgor pressure in yeast (9,10). Here we explore the hypothesis that increasing the membrane permeability at the endocytic site can locally reduce the turgor pressure and thus facilitate endocytosis.

The turgor pressure Π (10) pushes the plasma membrane against the cell wall and thus helps the cell maintain its shape and rigidity. It is generated through the larger internal concentration of glycerol, the main osmolyte in yeast, relative to the outside. The magnitude of Π is determined by the requirement that the chemical potential of the solvent (water) be constant across the membrane. For a dilute solution, the solvent chemical potential is $\mu(P,T,C) = \mu_0(P,T) - (C/C_{\text{solvent}})k_BT$ (11), where P is pressure; T is temperature; and C and C_{solvent} are the solute and solvent concentrations, respectively. The chemical potential varies with pressure according to $\partial\mu_0(P,T)/\partial P = 1/N_A C_{\text{solvent}}$ (11), where N_A is Avogadro's number and C_{solvent} is given in molar units. Thus the constancy of μ implies (here we have ignored possible changes in the concentrations resulting from pressure variations, because pressure changes in cells are much smaller than the gigapascal bulk modulus of water) that between any two points,

$$\Delta P = N_A k_B T \Delta C. \quad (1)$$

If the points are on opposite sides of the membrane, this implies that the turgor pressure is

$$\Pi = N_A k_B T \Delta C, \quad (2)$$

Submitted June 24, 2016, and accepted for publication October 13, 2016.
*Correspondence: aec@wustl.edu
Editor: James Keener.
http://dx.doi.org/10.1016/j.bpj.2016.10.040

where $\Delta C = C_{in} - C_{out}$ is the concentration difference across the membrane. In the scenario treated here, where a permeable patch leads to large concentration gradients inside the cell, Eq. 1 implies corresponding internal gradients of the pressure. Thus pressure does not equilibrate, even at long times, as long as the concentration gradient is maintained by the continuing production of osmolyte inside the cell. The pressure gradient does not cause macroscopic fluid flow, because there are additional forces on water molecules due to the osmolyte concentration gradient. The situation is analogous to that of water in a swimming pool. The pressure is greater at the bottom, but there is no macroscopic flow because the water molecules at the bottom have lower gravitational potential energy. In this case, the gravitational potential energy variation is replaced by variation in the free energy of water molecules resulting from the inhomogeneous osmolyte concentration.

Can established mechanisms, including curvature-generating proteins and actin polymerization, provide enough force to overcome the turgor pressure barrier? The driving forces from curvature-generating proteins and actin, along with opposing forces from surface tension and turgor pressure, are encapsulated in the Helfrich membrane deformation energy:

$$U = \int_S \left[2\kappa(H - H_0)^2 + \sigma - f_{actin} z\right] dS + \Pi V. \qquad (3)$$

Here κ is the bending modulus, Π is the turgor pressure, dS is an element of membrane area, V is volume of the invagination, H is the mean curvature, H_0 is the spontaneous curvature, σ is the surface tension, z is the inward displacement of the membrane, and f_{actin} is the pulling force density from actin. We estimate whether it is energetically favorable for a hemispherical invagination of radius of $R_i = 30$ nm (12) to form in the presence of accepted values of the turgor pressure. We take $\kappa = 285\ k_B T$ (13), and $\Pi = 0.6$ MPa as an average over a number of measurements (14–19). Then the stabilizing contribution from the curvature-generating proteins is $= -2\pi R_i^2 \kappa / R_i^2 = -1800\ k_B T$ (the negative of the curvature energy of the flattened membrane), while the opposing contribution from the turgor pressure is $(2\pi/3) R_i^3 \Pi = 8250\ k_B T$, leaving $8250\ k_B T - 1800\ k_B T = 6450\ k_B T$ to be supplied by actin pulling forces.

It is unlikely that actin polymerization can supply such a large energy. The above calculation suggests that ~22% of the opposing force from turgor pressure is canceled by the curvature-generating proteins, leaving a residual pressure of ~0.47 MPa to be generated by actin polymerization. This corresponds to a total force of $0.47\ \text{MPa} \times \pi(30\ \text{nm})^2 = 1300$ pN. This force must come from the polymerization of actin filaments around the invagination (4,5). The number of growing actin filaments is estimated to be 100–150 (20), so forces of ~10 pN per filament would be required. But the stall force estimated for a 2 μM free actin concentration A (20) is only $f_{stall} = k_B T/\delta \ln(A/A_c) \simeq 5$ pN (21), using a critical concentration of 0.1 μM (22) and a polymerization step size $\delta = 2.7$ nm. Thus actin polymerization cannot generate the 10 pN per filament force required. The 10 pN estimate is sensitive to the number of growing filaments; a filament number that is two to three times larger than the estimated value would reduce the force per filament below the stall force. However, it is unlikely that the growing-filament number exceeds our estimate. Sirotkin et al. (23) estimated the upper bound of the number of growing filaments to be 140, by subtracting the number of capping protein molecules present from the number of Arp2/3 molecules, where the latter number was assumed to correspond to the number of actin filaments. Berro et al. (24) estimated only eight growing filaments on the basis of polymerization-dynamics experiments.

Previous work has also suggested that known mechanisms of actin polymerization are too weak to drive endocytosis. A finite-element calculation (4) found that the actin polymerization pressure was too small to overcome the turgor pressure, and that overcoming a turgor pressure of just 0.1 MPa requires an actin network stiffer than any that have been studied to date. Another calculation based on membrane elasticity theory and an actin point force suggested that the required force is even larger than our estimate (5). Finally, calculations using somewhat different approaches (10) found it implausible that actin polymerization can overcome the turgor pressure. We note, however, that the insufficiency of actin polymerization forces cannot be taken as rigorously proved, because there are substantial uncertainties in all of the quantities used to estimate the slowing of polymerization.

Thus for endocytosis to proceed against current estimates of the turgor pressure, rather extreme assumptions about actin polymerization forces and elastic properties would likely have to hold. A local reduction of the turgor pressure, in the vicinity of the endocytic site, provides a possible alternative to unphysically large actin polymerization forces.

MATERIALS AND METHODS

To see how much the turgor pressure might be reduced by a physically reasonable distribution of membrane channels, we solve two diffusion-based models of yeast membranes with locally enhanced permeability. The assumption of a locally enhanced permeability is supported by the observation of patches of the glycerol transporter Fps1 at the cell membrane in budding yeast (25). However, it is not known whether these patches coincide with endocytic sites.

Assumptions

Model 1 assumes a spherical cell with the membrane permeability increased in a narrow circular patch (see Fig. 1). Glycerol, the main osmolyte, is produced at a rate, constant in both time and space within the cell.

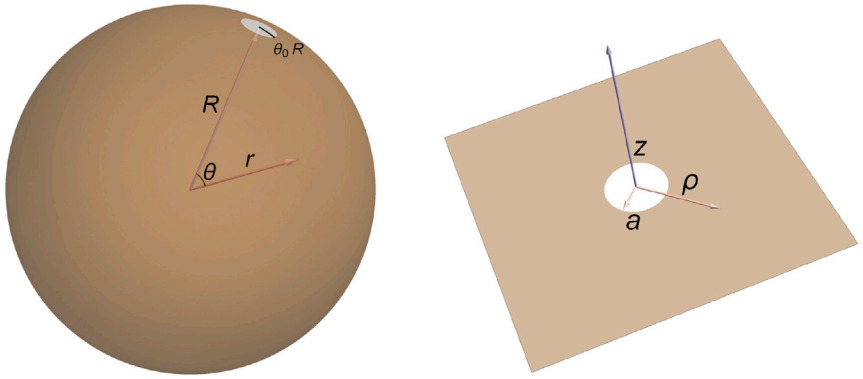

FIGURE 1 Model 1, spherical cell with permeable patch; Model 2, plane with hole. To see this figure in color, go online.

The turgor pressure is determined by a balance between production and leakage. We assume azimuthal symmetry about the center of the permeable patch, and define the angle θ relative to this center. To optimize numerical convergence, we assume a smoothly varying permeability profile of the form $P(\theta) = P_a + P_b \exp[-\theta^2/(\Delta\theta)^2]$. For ease of comparison with our analytic Model 2 below, we also fit this to a model with a discontinuous permeability, having the form:

$$P(\theta) = \begin{cases} P_1 & \theta < \theta_0 \\ P_2 & \theta > \theta_0 \end{cases}. \tag{4}$$

The coefficients $P_{a,b}$ of the continuous permeability are chosen so that $P(0) = P_1$, $P(\pi) = P_2$. We then choose $\Delta\theta$ to optimize the fit to the discontinuous permeability. For conceptual clarity, we present our results below in terms of θ_0, P_1, and P_2.

Model 2 assumes an infinite, impermeable plane, with two long-distance concentrations C_{in}, C_{out}, and a perfectly permeable hole of radius a (we take $C_{\text{out}} = 0$ in our results presented below). These approximations allow for an analytic solution. Model 2 is a good approximation to Model 1 in certain parameter ranges, because the size of the permeable patch is small relative to the size of the cell, and the permeability in the middle of the patch is much larger than that far from the patch. In relating Models 1 and 2, we find that a good match is obtained by taking $a = 1.3\ \theta_0 R$, where R is the cell radius.

In both models, the varying concentrations of glycerol cause a spatially varying hydrostatic pressure because of the constraint of spatially constant chemical potential. The effects of the pressure on the water and glycerol diffusion coefficients, and possible pressure gradient terms in the glycerol current, are assumed small and are neglected.

Equations

In Model 1, the steady-state distribution of glycerol $C(\mathbf{r})$ is governed by the reaction-diffusion equations:

$$D\nabla^2 C(\mathbf{r}) + \alpha = 0\ (r < R), \tag{5}$$

$$D\nabla^2 C(\mathbf{r}) = 0\ (r > R), \tag{6}$$

where r is distance from the center of the cell, D is the diffusion coefficient, and α is the rate of glycerol production. The boundary conditions, taking into account the definition of the permeability as the ratio of current density to concentration discontinuity, are

$$\begin{cases} \left(\dfrac{\partial C}{\partial r}\right)_{r=R} = -P(\theta)(1/D)\Delta C, \\ \lim_{r\to\infty} C(r,\theta) = 0 \end{cases} \tag{7}$$

where $\Delta C = \lim_{\epsilon\to 0}[C(R-\epsilon,\theta) - C(R+\epsilon,\theta)]$ is the concentration discontinuity.

Because Model 2 assumes asymptotic concentrations rather than a production rate, there is no α term, and we have

$$D\nabla^2 C(\mathbf{r}) = 0. \tag{8}$$

The boundary conditions are

$$\begin{cases} C(z = 0^+, \rho) = C(z = 0^-, \rho) \text{ for } \rho < a \\ \left(\dfrac{\partial C}{\partial z}\right)_{z=0} = 0 \text{ for } \rho > a \\ \lim_{z\to\infty} C(z,\rho) = C_{\text{out}} \\ \lim_{z\to-\infty} C(z,\rho) = C_{\text{in}} \end{cases}. \tag{9}$$

Here z is the coordinate perpendicular to the plane (at $z = 0$), and ρ is the radial coordinate, measured from the z axis going through the center of the hole.

Solution of Model 1

Model 1 has the general solution

$$C(r,\theta) = -\frac{\alpha}{6D} r^2 + \sum_{l=0}^{\infty} C_l (r/R)^l P_l(\cos\theta) \quad r < R, \tag{10}$$

$$C(r,\theta) = \frac{\alpha R^3}{3Dr} - \sum_{l=1}^{\infty} \frac{l C_l}{l+1} (R/r)^{l+1} P_l(\cos\theta) \quad r > R. \tag{11}$$

Here we have expanded $P(\theta)$ as $P(\theta) = \sum_{l=0}^{\infty} A_l P_l(\cos\theta)$, where $P_l(\cos\theta)$ is the Legendre polynomial of order l and $A_l = [(2l+1)/2] \int d\theta \cos(\theta) P(\theta) P_l(\cos\theta)$; the relationship between the coefficients of P_l for $r > R$ and $r < R$ results from the continuity of $\partial C/\partial r$ at R. Integrating the first of expressions in Eq. 7 with $P_k(\cos\theta)$ and employing the orthogonality properties of the Legendre polynomials, we see that the C_l in Eqs. 10 and 11 satisfy

$$(1/D) \sum_{l=0}^{\infty} \sum_{m=0}^{\infty} \frac{2l+1}{l+1} C_l I_{\text{lmk}} A_{\text{m}} + \frac{k C_k}{R} \frac{2}{2k+1} = \frac{\alpha R^2}{2D} \frac{2A_k}{2k+1} + \frac{2\alpha R}{3D} \delta_{k0}, \tag{12}$$

where (in terms of the Wigner-3j symbol) (26):

$$I_{\mathrm{lmk}} = \int_{-1}^{1} d(\cos\theta) P_l(\cos\theta) P_m(\cos\theta) P_k(\cos\theta) = 2\begin{pmatrix} l & m & k \\ 0 & 0 & 0 \end{pmatrix}^2. \quad (13)$$

The 3j-symbols are nonzero only when $J = l + m + k$ is even, and were calculated from the identity

$$\begin{pmatrix} l & m & k \\ 0 & 0 & 0 \end{pmatrix} = (-1)^g \sqrt{\frac{(2g-2l)!(2g-2m)!(2g-2k)!}{(2g+1)!}} \frac{g!}{(g-l)!(g-m)!(g-k)!}, \quad (14)$$

where $g = J/2$.

To calculate the coefficients numerically, we approximate the infinite-dimensional system with one of finite dimension by truncating the summation at L coefficients, resulting in an $L \times L$ system (600 by 600, unless otherwise mentioned) to be solved for the coefficients C_l. The A_l were obtained as numerical integrals. We find that the solution to the truncated system converges as L increases. As a measure of the convergence of the solution we used the variation of the concentration difference across the membrane. The choice of $L = 600$ is justified by Fig. 2, which indicates that the solution converges for $\sim L > 150$ for the baseline parameters; for the slowest converging cases, the error is <1%. Thus we see that the approximate solution of Eqs. 4 and 5 provides an accurate solution to the problem.

Solution of Model 2

The solution to Model 2 uses the solution for the case $C_{\mathrm{in}} = -C_{\mathrm{out}}$ given in Crank (27). We summarize the method used to obtain the solution. The approach uses the correction to the solution that would hold if no hole were present. The sign of the correction is opposite on each side. We thus have

$$C(\mathbf{r}) = \begin{cases} C_{\mathrm{in}} - \tilde{C}(z,\rho) & z < 0 \\ C_{\mathrm{out}} + \tilde{C}(z,\rho) & z > 0, \end{cases} \quad (15)$$

where $\tilde{C}(z,\rho)$ is the correction for $z > 0$.

At $z = 0$, the boundary conditions (Eq. 9) require that $C(\mathbf{r})$ be continuous inside the hole, while outside the hole $\partial C/\partial z = 0$. In terms of the correction, this becomes $\tilde{C}(0^+,\rho) = (1/2)(C_{\mathrm{in}} - C_{\mathrm{out}})$ for $\rho < a$, $\left(\frac{\partial \tilde{C}(z,\rho)}{\partial z}\right)_{z=0} = 0$ for $\rho > a$.

Equation 8 for $\tilde{C}$ is solved in the Supporting Material by an expansion in Bessel functions. The result, for $C_{\mathrm{out}} = 0$, is

$$C(\mathbf{r}) = \begin{cases} C_{\mathrm{in}} - \frac{C_{\mathrm{in}}}{\pi} \tan^{-1}\left(\sqrt{\frac{2}{\zeta + \lambda}}\right) & z < 0 \\ \frac{C_{\mathrm{in}}}{\pi} \tan^{-1}\left(\sqrt{\frac{2}{\zeta + \lambda}}\right) & z > 0 \end{cases}, \quad (16)$$

where $\lambda = (1/a^2)(\rho^2 + z^2 - a^2)$ and $\zeta = (\lambda^2 + (4z^2/a^2))^{1/2}$.

This model is expected to reproduce the spherical-model results in certain limits. In the spherical model there is a finite discontinuity across the hole, while in the planar model, the concentration is continuous. In the spherical model, there is some membrane current outside the patch, whereas in the planar model there is none. Finally, the spherical model has a curved geometry, while that in the planar model is flat. We thus expect the planar model to approximate the spherical one well only if $P_1 a/D$ is large, $P_2 R/D$ is small, and a/R is small. The second and third conditions hold for all our parameter sets, but the first holds only at the upper end of the values of P_1 that we have treated.

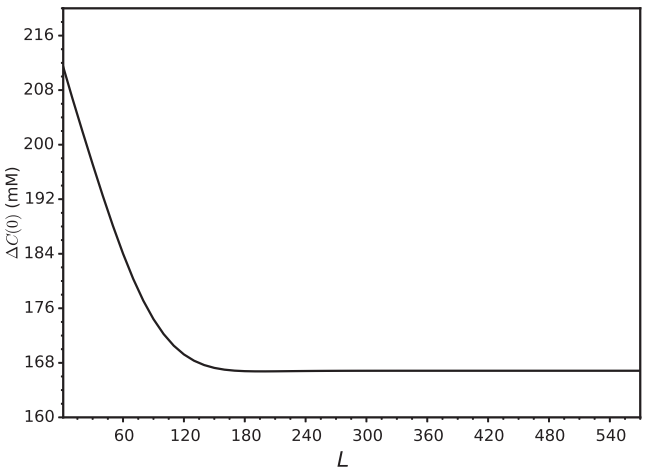

FIGURE 2 Concentration difference at $\theta = 0$ versus L, using baseline parameters. L is the numerical cutoff for Eq. 12, and the plot shows that the results are well converged already when $L > 150$.

RESULTS

Model 1—spherical cell

The parameter values are given in Table 1. We vary θ_0 and P_1 because their values are poorly known. In choosing our range of values for θ_0, we note that the radius of the invagination is ~30 nm, corresponding to $\theta = 0.01$, while the radius of the ribosome-free zone around the invagination indicating the presence of F-actin is ~100 nm (12), corresponding to $\theta = 0.033$. The value of θ_0 is likely not much smaller than the radius of the invagination region, because the turgor pressure needs to be reduced over the whole invagination region. However, portions of the permeable region outside the invagination region can contribute to the turgor pressure reduction in the invagination region. Thus

TABLE 1 Parameter Values for Spherical-Cell Model

Cell radius, R	3 μm	(31)
Patch angular radius, θ_0	0.02 radians (varied)	(12)
Single-channel permeability, P_c	1.0×10^{-13} cm^3/s	(28)
Patch permeability, P_1	4×10^{-2} cm/s (varied)	From assumed spacing of 16 nm
Membrane permeability, P_2	4×10^{-6} cm/s	(30)
Glycerol diffusion coefficient, D	1.1×10^{-6} cm^2/s	10% of value in Lide (32)
Turgor pressure, Π	0.6 MPa	(15)
Glycerol production rate, α	30 mM/s	Determined from Π

For parameters that are varied, we give baseline values used in most of the plots.

we used a range of θ_0 values between 0.006 and 0.03. As a baseline value, we use $\theta_0 = 0.02$.

We base our range of values of P_1 on P_c, the single-channel permeability of a channel protein such as Fps1 in *S. cerevisiae*, which can transport glycerol to the outside of the cell. We are not aware of experimental estimates of the single-channel permeability of Fps1 or other glyceroporins. The value of P_c was thus determined as being in the middle of the range of water permeability values quoted in Yang and Verkman (28), noting that glycerol permeability values are similar to water permeability values (29). To estimate P_1 from P_c, we assume a constant density of channels. The permeability is taken to be

$$P_1 = (1 - n_c A_c) P_2 + n_c P_c \approx n_c P_c, \qquad (17)$$

where $n_c = N_c/A_p$ is the channel number density per unit area and A_c is the area per channel. The term with the minus sign is the total area taken up by the channels, and is included to avoid double-counting of the permeability. The second relation holds approximately because $P_1 \gg P_2$. Our range of P_1 values corresponds to values of the center-to-center channel distance ranging down to 10 nm; the baseline value of 4×10^{-2} cm/s corresponds to a spacing of 16 nm. Because the measured global permeability values (30) include the effects of channels such as Fps1, and P_2 corresponds to regions of the membrane where channels are depleted by clustering into patches in other regions, we choose our value of P_2 at the lower end of the values quoted in Smith (31).

In choosing D, we assumed a cytoplasmic value 10 times smaller than the water value given in Lide (32). This value is somewhat uncertain, and we treat the effects of varying D in the Discussion. The production rate α was obtained by imposing the constraint $k_B T\, N_A\, \Delta C(\pi) = \Pi$. We note that because all concentrations in the model are proportional to α, changes in α will not affect fractional reductions in turgor pressure.

Fig. 3 *a* shows the typical behavior of the concentration as a function of radius, going from inside the cell, through the cell membrane $r = 3$ μm, and continuing outside the cell. Each of the curves shows a dropoff in C approaching the membrane from the inside, with a corresponding feature outside the membrane. This leads to a reduction in the discontinuity ΔC, which causes a corresponding reduction in the turgor pressure Π according to Eq. 2. As seen in the figure, the effect is smaller when the patch width θ_0 is reduced and larger when P_1 is increased. Fig. 3 *b* shows ΔC as function of angle relative to the patch center. The maximum reduction in ΔC, 31%, occurs at the center $\theta = 0$ of the patch, but the effect is also pronounced for $\theta > \theta_0$; at $\theta = \theta_0$ the reduction is 22%. Thus significant local reductions in turgor pressure occur for our baseline parameter values.

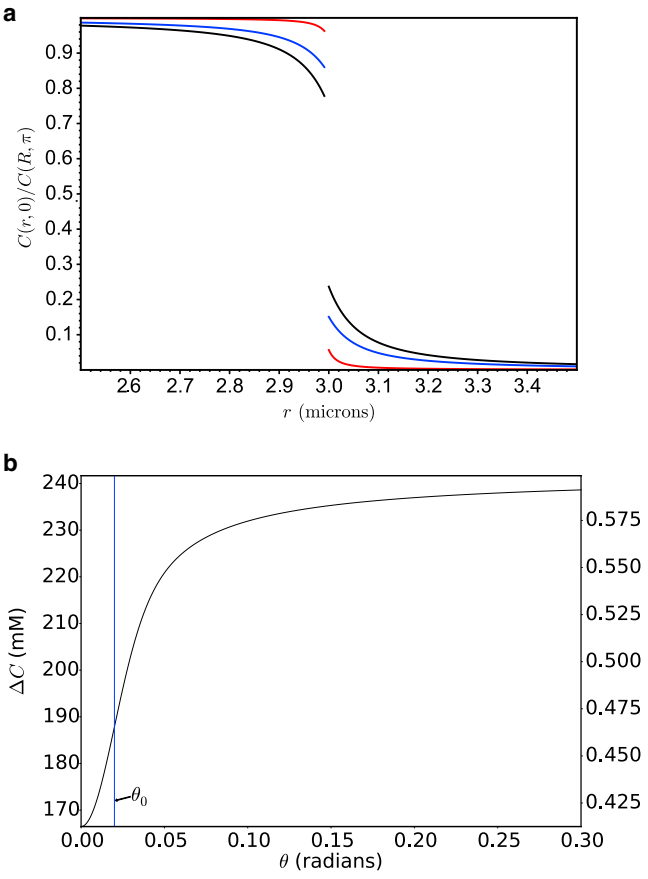

FIGURE 3 (*a*) Concentration versus radius for various values of θ_0 and P_1. Parameters are baseline, except for the following: (*red line*) $\theta = 0.006$, (*black line*) $P_1 = 0.08$ cm/s. (*b*) Concentration difference versus angle for baseline parameters. To see this figure in color, go online.

Fig. 4 *a* shows the concentration difference reduction as a function of P_1 for a range of values of θ_0. All the curves have a similar shape, with the reduction becoming larger as θ_0 increases.

Scaling form for concentration difference reduction

The model has two small dimensionless parameters: $P_2R/D = 1.1 \times 10^{-3}$, and $a/R = 1.3\ \theta_0 \approx 0.008 - 0.04$. The smallness of these parameters suggests that the ratio of ΔC at the center of the patch to ΔC at the other end of the cell, $\delta c = |\Delta C(0)/\Delta C(\pi)|$, might depend only weakly on P_2 and R, provided that a is kept constant. As mentioned above, there is no dependence on α, because increasing α by a certain factor changes both $\Delta C(0)$ and $\Delta C(\pi)$ by the same factor. If P_2 and R have only weak effects on δc, then δc will be determined almost entirely by P_1, a, and D. There is only one dimensionless combination of these parameters that could enter δc, so a relation of the form

$$\delta c = f(P_1 a/D) \tag{18}$$

should hold to high accuracy, where f is an unknown function. This relation makes two predictions: (1) That δc is independent of P_2; we have tested this prediction by increasing and decreasing P_2 by a factor of two, and as expected, found changes of only 0.5%. (2) If $P_1^{50\%}$ is the value of P_1 required to achieve a 50% reduction in ΔC, so that $\delta c = 0.5$, then $P_1^{50\%} \propto 1/a$. Our test of this prediction is given in Fig. 4 *b*, which shows that the relationship

$$P_1^{50\%} = 0.44\, D/a \tag{19}$$

holds to an accuracy of 2%.

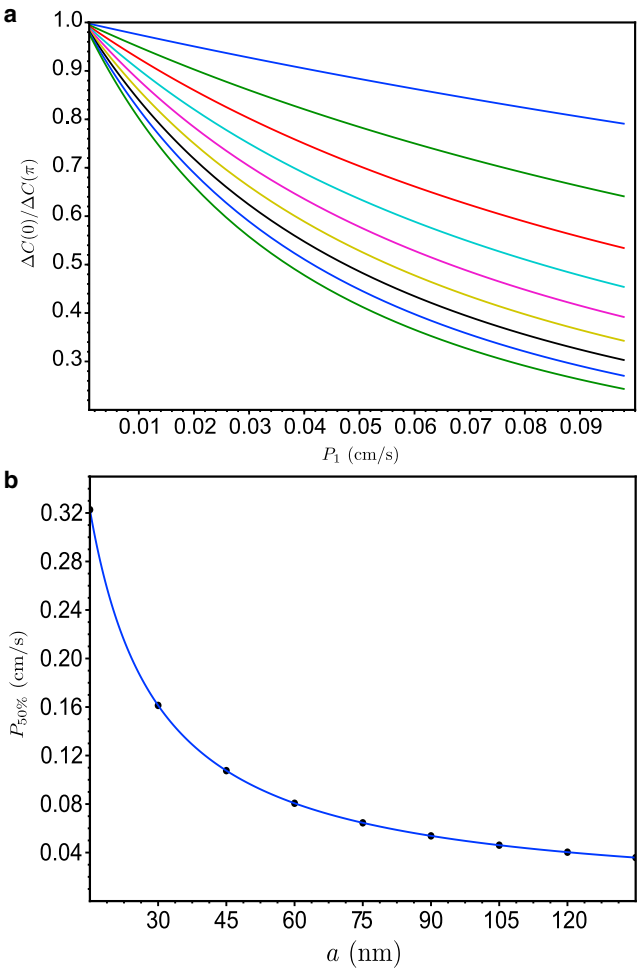

FIGURE 4 (*a*) Concentration difference at $\theta = 0$, relative to bulk membrane value, versus permeability. Curves (*top* to *bottom*) have θ_0 ranging from 0.006 to 0.03, with spacing 0.003. (*b*) Value of P_1 required to reduce $\Delta C(0)/C(\pi)$ by 50%, as function of patch radius a. (*Solid line*) Fit of form $P_{50\%} = 0.44\, D/a$. To see this figure in color, go online.

Model 2—planar geometry

Fig. 5 *a* shows results for Model 2. It is seen that the concentration drops over a range of values of z comparable to the hole width a. We compared these results to those for the spherical model by identifying a with $1.3\ \theta_0 R$, z with $r - R$, C_{in} with the concentration at the center of the cell, and taking $C_{\text{out}} = 0$; the prefactor in a optimized the agreement between the models. We also used a large value of P_1, to optimize agreement with the planar case. The agreement is quite good, with the main difference being that the discontinuity ΔC vanishes in the planar model while it has a small nonzero value in the spherical model.

Analytic theory of patch current and reduction in concentration difference

For the purposes of finding a simple formula for the reduction of $\Delta C(0)$ in Model 1, we first develop an expression for the total current I through the patch. We calculate I in Model 2 as a starting point. Inspection of Eq. 16 shows that if $C(\vec{r}, \rho)$ is the solution for a hole of radius a, then $C(\vec{r}/\eta, \rho/\eta)$ is the solution for a hole of radius ηa. In other words, the spatial scale of the solution is proportional to a. Because the current density in the hole is proportional to $D\partial C/\partial z \propto a^{-1}$, and the area of the hole is proportional to a^2, it follows that $I \propto a$. Inserting the additional proportionality to C_{in} and D, we obtain

$$I = \nu D a\, C_{\text{in}}, \tag{20}$$

where $\nu = 1.98$ is obtained numerically from the solution given in Eq. 16.

We next calculate the current I through the permeable patch in Model 1 in two limiting cases. We assume that the permeability has the constant value P_1 over a disk of radius a, and the value P_2 outside that disk, and use $\Delta C(\pi)$ as a measure of the bulk concentration discontinuity.

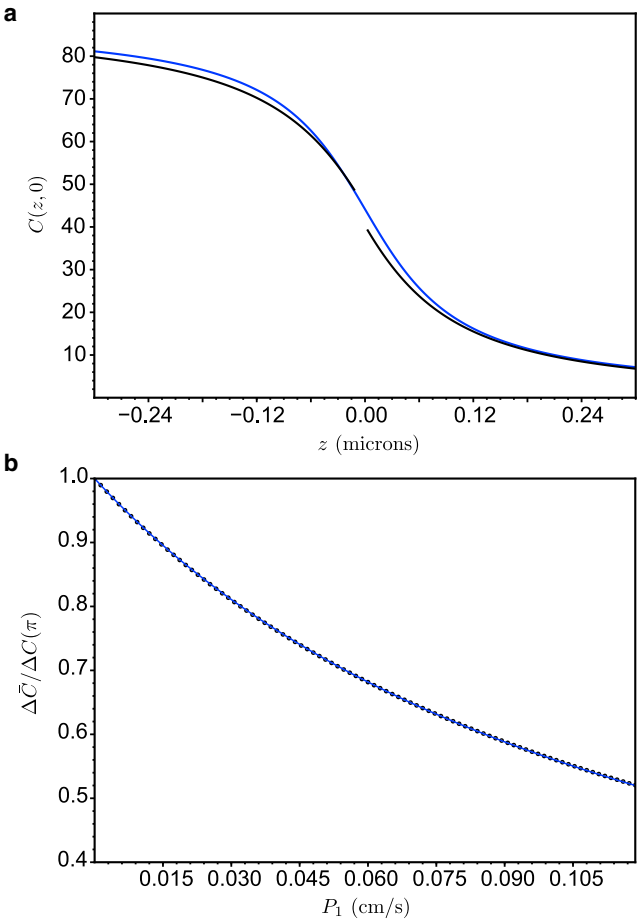

FIGURE 5 (*a*) Planar model concentration (*black*) and spherical model concentration (*blue*) along line through center of hole/patch, for $P_1 = 1.0$ cm/s and $a = 1.3\ \theta_0\ R = 78$ nm. In spherical model, plot is radial and $r = R + z$. (*b*) Reduction in average concentration over a permeable patch as function of P_1. Dots are numerical results and line is analytic theory from Eq. 22, using $a = 1.3\ \theta_0\ R$ and a fitted value $\nu = 2.9$. To see this figure in color, go online.

In the limit of low permeability $P_1 a/D \ll 1$, ΔC should be constant over the interior surface of the cell, because diffusion will eliminate concentration gradients. Then $I = P_1 \pi a^2 \Delta C(\pi)$. In the high-permeability limit $P_1 a/D \gg 1$, the planar model is applicable, and we use Eq. 20. We identify C_{in} in Eq. 20 with $\Delta C(\pi)$, because the concentration outside the cell at $\theta = \pi$ is very small, so that $C \simeq \Delta C$. Thus $I = \nu D a \Delta C(\pi)$.

To construct a formula for intermediate values of $P_1 a/D$, we view osmolytes flowing through the patch as experiencing two resistances in series, corresponding to diffusion to the patch and subsequent permeation of the patch. Each process is defined by a resistance $\Delta C(\pi)/I$. The resistance to diffusion is the total resistance for very large P_1, which from the discussion above is $1/\nu D a$. Similarly the resistance to permeation is obtained by taking $P_1 a/D$ very small, and equals $1/P_1 \pi a^2$. Adding the resistances, we obtain $\Delta C(\pi)/I = 1/\nu D a + 1/P_1 \pi a^2$, or

$$I = \Delta C(\pi) \frac{\nu P_1 D \pi a^2}{\nu D + P_1 \pi a}. \tag{21}$$

Finally, I is related to $\Delta\overline{C}$, the average of ΔC over the permeable patch. By the definition of the permeability, $I = \pi a^2 P_1 \Delta\overline{C}$. Putting this into Eq. 21, we have

$$\frac{\Delta\overline{C}}{\Delta C(\pi)} = \frac{1}{1 + \dfrac{\pi P_1 a}{\nu D}}. \tag{22}$$

As seen in Fig. 5 *b*, this formula gives an excellent description of the simulation results, provided that we use a fitted value of $\nu = 2.9$. It emphasizes the role of the key dimensionless parameter $P_1 a/D$.

DISCUSSION

Extent of turgor pressure reduction in yeast

To evaluate the potential relevance of local turgor pressure reduction to endocytosis in yeast, we estimate a plausible value of P_1. Superresolution imaging of aquaporin clusters in brain cells (33) found an area of 36 nm^2 per aquaporin, corresponding to a center-to-center spacing of 6 nm. Because endocytic protein patches contain a number of other membrane proteins, we use a conservative estimate of a 10 nm center-to-center spacing, corresponding to a channel density n_c of 10^{12} cm^{-2}. Taking the single-channel permeability to be 10×10^{-13} cm^{-3} (Table 1), we find $P_1 = 0.1$ cm/s. Above in Fig. 4 *b*, we found that for this value of P_1, a 50% reduction in the turgor pressure will occur as long as the patch radius is 45 nm or greater. Thus patches only slightly larger than the invagination size can reduce the turgor pressure significantly. A patch of 45 nm would contain ~60 channels. This number is comparable to the counts of the coat proteins known to be important for endocytosis in budding yeast. For example, the maximum count of the linker protein Sla2 is ~50 (34). In addition, this channel cluster size is similar in magnitude to the 35-channel aquaporin clusters previously observed in Smith and Verkman (33).

Equation 22 shows that the turgor pressure reduction is enhanced if D is smaller than the value given in Table 1. It will also be enhanced if diffusion in the cell wall outside the membrane is slower than in the cytoplasm. Because treating a cell wall with finite thickness would be significantly more complicated than the calculations we have done, we instead have considered a model in which the diffusion coefficient is reduced uniformly outside the membrane. This corresponds to changing the boundary conditions in Eqs. 7. We find that if the outside value of the diffusion coefficient is reduced by 50%, $P_{50\%}$ is reduced by 55%.

For the turgor pressure reduction to facilitate endocytosis, it must persist when the membrane is bent inward, up to the

point where a tubule forms and late-arriving curvature-generating proteins assist the process. We see no mathematically practical way of performing the calculations for an inward-bent membrane. However, we note that diffusion currents in general are much more sensitive to the maximum size of their target than to its shape. For example, the diffusion current to a perfectly absorbing cylindrically symmetric ellipsoid of semimajor axis a and semiminor axis b, with $a \gg b$, differs from the current to a perfect absorbing sphere of radius a by only a logarithmic factor of $(1/\ln(2a/b))$ (35); the current to a disk of radius a differs from that to a sphere of radius a by only a factor of $(2/\pi)$ (27). Therefore the current I from the inside of the cell through the permeable patch should depend mainly on the maximum dimension of the patch rather than its deformation. Further, $I = N_c P_c \Delta\overline{C}$, where N_c is the number of channels, P_c is the single-channel permeability, and $\Delta\overline{C}$ is the average concentration difference across the membrane over the area of the patch. If N_c and P_c are constant, then $\Delta\overline{C}$ will also be relatively independent of patch deformation. Thus the turgor pressure reduction will persist even when the membrane is bent inwards, until it forms a tubule.

The presence of permeable patches can also cause a substantial decrease in the bulk turgor pressure if α is unaffected by the patches. Using the maximum estimate of $P_1 = 0.1$ cm/s, together with the corresponding patch radius of 45 nm, we find a global turgor pressure reduction of 52%. This does not affect our key results because we focus on the ratio of the turgor pressure at the permeable patch to that in other parts of the cell. Because the permeable patch is small, the measured turgor pressure corresponds to the calculated value away from the patch. The effect on the bulk turgor pressure will be reduced if P_2 is larger than is assumed in Table 1, because a lower fraction of the total osmolyte current will flow through the patch. It will also be reduced if D is smaller, because this reduces the required values of P_1 and a, according to Eq. 19.

Relation to experiments

We are not aware of experiments currently in the literature that can test the hypothesis of local turgor pressure reduction in yeast. However, the efficiency of invagination is greatly reduced in deletion mutants of the channel Fps1 (9), an effect that could increase turgor pressure either locally or globally. Fps1 localizes in membrane patches (25). To establish the extent of channel clustering at endocytic sites, one could use two-color fluorescence imaging to measure colocalization of Fps1 and with endocytosis markers such as the early scaffold protein Ede1 or the polymerized-actin proxy Abp1. Colocalization of channel patches with endocytic proteins would indicate that the turgor pressure is locally reduced around the endocytic site. Appearance of the channels before Ede1 would suggest that the channels have a function in marking the endocytic site. On the other hand, appearance of the channels after Abp1 could mean that polymerized actin is important for recruiting the channels. Such a possibility is suggested by the documented effects of polymerized actin on channel dynamics in other types of cells (36–38). If the channel patches do colocalize with endocytic sites, superresolution measurements of the distribution of channels could provide a concrete test of our hypothesis.

Previous experiments have demonstrated that the effect described here, variations of osmotic pressure difference across the membrane caused by variations in channel density, does function on larger spatial scales. For example, segregation of aquaporins and Na^+/H^+ channels to the leading edge of cancer cells led to osmolyte concentration gradients over the length of the cell, which in turn created internal pressure gradients that drove migration through artificial channels (39). Here we predict that gradients of osmolytes over much smaller distances, caused by higher densities of channels, will lead to osmotic pressure variations over these smaller distances.

Application to plant cells

The high turgor pressure in plants also poses conceptual difficulties in rationalizing the mechanobiology of endocytosis, and some early articles actually doubted the existence of the process for this reason (40,41). Endocytosis in plants has some parallels to the process in yeast, in particular its polymerized-actin dependence (42,43). The difficulties of overcoming high turgor pressure in plants by an actin-dependent process might thus be eased by a local turgor pressure reduction mechanism like that we discuss here for yeast.

Alternative mechanisms

Several other possible mechanisms might deal with the difficulty of generating sufficient force via actin polymerization and curvature-generating proteins. A calculation based on the total number of type-I myosins in fission yeast (10), assuming that each one can generate 2 pN of force, suggested that they could overcome the turgor pressure, but only over a smaller region of radius 10 nm. The geometric arrangement of myosins that would supply forces with the correct orientation and distribution is also not known. One possibility is that the myosins turn actin filaments into "superpolymerizers" by 1) binding the filaments to the membrane and 2) moving to the growing tip of the actin filament after each polymerization event, keeping it far enough from the membrane that new subunits can be added freely (44). In this hypothesis, myosins act somewhat like formins, which drive processive elongation of actin filaments while bound to the membrane. An alternate possibility is one analogous to tubulation of giant unilamellar vesicles driven by type-1 myosin (45), where the driving

force for tubulation came from myosin motion along a preexisting actin scaffold. We are not aware of measurements of the force-generating capability of yeast type-1 myosins, but mammalian type-1 myosins are able to generate up to 5 pN of force per molecule (46). It is also possible that there are growing actin filaments that were not detected in the previous filament counts based on Arp2/3 complex-mediated branching (20,23). These could, for example, be generated by domains on the actin nucleator Las-17 that act independently of the Arp2/3 complex (47).

It has also been suggested that polymerization of actin filaments along the membrane could generate much larger forces in a wedgelike geometry (48). The transmission of such forces to the membrane would require a very stiff actin gel (4). There is no proof that a gel with such properties exists, but the high cross-linking fraction in endocytic actin patches could make them much stiffer than other forms of polymerized actin.

Another possibility is that curvature-generating proteins could be providing a very large fraction, say 90%, of the force overcoming turgor pressure. However, if this were the case, one would expect that the large heterogeneity between cells, and between endocytic events in the same cell, would often lead to the curvature-generating proteins exerting sufficient force to drive the process by themselves, in the absence of actin polymerization. Correlative electron-microscopy and light-microscopy experiments (12) have shown that this is not the case: substantial membrane deformation seldom or never occurs without polymerized actin.

Finally, the global turgor pressure could be overestimated. The turgor pressure is typically measured indirectly (15), by exposing the cell to increasing solute concentrations and measuring the volume change. The turgor pressure is proportional to the minimal external solute concentration increase that causes the cell wall to collapse, on the assumption that the membrane collapses at zero turgor pressure. These methods could overestimate the turgor pressure because cells react to increasing external solute concentration by increasing the internal solute concentration, thus requiring higher external concentrations for collapse (25). Osmoregulation could also confound mechanically based turgor pressure measurements (16), if internal osmolytes are upregulated in response to force opposing cell growth. Direct methods using an indentor that penetrates the cell wall are impractical in yeast because of the small system size. But experiments in plant cells (14) have shown good consistency between indirect and direct methods. Therefore, for the global turgor pressure in yeast to be strongly overestimated, osmoregulation mechanisms in yeast would have to be more efficient than in plants.

SUPPORTING MATERIAL

Supporting Materials and Methods are available at http://www.biophysj.org/biophysj/supplemental/S0006-3495(16)31000-1.

AUTHOR CONTRIBUTIONS

J.K.S.-Z. collaborated on developing the mathematical formalism, implemented and performed the calculations, generated the figures, and collaborated on writing the article; and A.E.C. collaborated on developing the mathematical formalism and on writing the article, and supervised the project.

ACKNOWLEDGMENTS

We appreciate informative conversations with Elizabeth Haswell.

This work was supported by the National Institutes of Health (NIH) under grants No. R01 GM107667 and T32 EB018266-03.

REFERENCES

1. McMahon, H. T., and E. Boucrot. 2011. Molecular mechanism and physiological functions of clathrin-mediated endocytosis. *Nat. Rev. Mol. Cell Biol.* 12:517–533.
2. Kaksonen, M., C. P. Toret, and D. G. Drubin. 2006. Harnessing actin dynamics for clathrin-mediated endocytosis. *Nat. Rev. Mol. Cell Biol.* 7:404–414.
3. Galletta, B. J., and J. A. Cooper. 2009. Actin and endocytosis: mechanisms and phylogeny. *Curr. Opin. Cell Biol.* 21:20–27.
4. Carlsson, A. E., and P. V. Bayly. 2014. Force generation by endocytic actin patches in budding yeast. *Biophys. J.* 106:1596–1606.
5. Dmitrieff, S., and F. Nédélec. 2015. Membrane mechanics of endocytosis in cells with turgor. *PLOS Comput. Biol.* 11:e1004538.
6. Liu, J., Y. Sun, …, G. F. Oster. 2009. The mechanochemistry of endocytosis. *PLoS Biol.* 7:e1000204.
7. Jelerčič, U., and N. S. Gov. 2015. Pearling instability of membrane tubes driven by curved proteins and actin polymerization. *Phys. Biol.* 12:066022.
8. Zhang, T., R. Sknepnek, …, J. M. Schwarz. 2015. On the modeling of endocytosis in yeast. *Biophys. J.* 108:508–519.
9. Aghamohammadzadeh, S., and K. R. Ayscough. 2009. Differential requirements for actin during yeast and mammalian endocytosis. *Nat. Cell Biol.* 11:1039–1042.
10. Basu, R., E. L. Munteanu, and F. Chang. 2014. Role of turgor pressure in endocytosis in fission yeast. *Mol. Biol. Cell.* 25:679–687.
11. Landau, L. D., and E. M. Lifshitz. 1969. Statistical Physics, Vol. 5: Course of Theoretical Physics. Pergamon Press, Oxford, UK.
12. Kukulski, W., M. Schorb, …, J. A. Briggs. 2012. Plasma membrane reshaping during endocytosis is revealed by time-resolved electron tomography. *Cell.* 150:508–520.
13. Jin, A. J., K. Prasad, …, R. Nossal. 2006. Measuring the elasticity of clathrin-coated vesicles via atomic force microscopy. *Biophys. J.* 90:3333–3344.
14. Beauzamy, L., J. Derr, and A. Boudaoud. 2015. Quantifying hydrostatic pressure in plant cells by using indentation with an atomic force microscope. *Biophys. J.* 108:2448–2456.
15. Schaber, J., M. À. Adrover, …, E. Klipp. 2010. Biophysical properties of *Saccharomyces cerevisiae* and their relationship with HOG pathway activation. *Eur. Biophys. J.* 39:1547–1556.
16. Minc, N., A. Boudaoud, and F. Chang. 2009. Mechanical forces of fission yeast growth. *Curr. Biol.* 19:1096–1101.
17. Meikle, A. J., R. H. Reed, and G. M. Gadd. 1988. Osmotic adjustment and the accumulation of organic solutes in whole cells and protoplasts of *Saccharomyces cerevisiae*. *Microbiology.* 134:3049–3060.
18. Martinez de Marañon, I., P. A. Marechal, and P. Gervais. 1996. Passive response of *Saccharomyces cerevisiae* to osmotic shifts: cell volume variations depending on the physiological state. *Biochem. Biophys. Res. Commun.* 227:519–523.

19. Goldenbogen, B., W. Giese, …, E. Klipp. 2016. Dynamics of cell wall elasticity pattern shapes the cell during yeast mating morphogenesis. *Open Biol.* 6:160136.
20. Wang, X., B. J. Galletta, …, A. E. Carlsson. 2016. Actin-regulator feedback interactions during endocytosis. *Biophys. J.* 110:1430–1443.
21. Hill, T. L., and M. W. Kirschner. 1982. Bioenergetics and kinetics of microtubule and actin filament assembly-disassembly. *Int. Rev. Cytol.* 78:1–125.
22. Pollard, T. D. 1986. Rate constants for the reactions of ATP- and ADP-actin with the ends of actin filaments. *J. Cell Biol.* 103:2747–2754.
23. Sirotkin, V., J. Berro, …, T. D. Pollard. 2010. Quantitative analysis of the mechanism of endocytic actin patch assembly and disassembly in fission yeast. *Mol. Biol. Cell.* 21:2894–2904.
24. Berro, J., V. Sirotkin, and T. D. Pollard. 2010. Mathematical modeling of endocytic actin patch kinetics in fission yeast: disassembly requires release of actin filament fragments. *Mol. Biol. Cell.* 21:2905–2915.
25. Tamás, M. J., K. Luyten, …, S. Hohmann. 1999. Fps1p controls the accumulation and release of the compatible solute glycerol in yeast osmoregulation. *Mol. Microbiol.* 31:1087–1104.
26. Johansson, H. T., and C. Forssén. 2016. Fast and accurate evaluation of Wigner 3 j, 6 j, and 9 j symbols using prime factorization and multi-word integer arithmetic. *SIAM J. Sci. Comput.* 38:A376–A384.
27. Crank, J. 1979. The Mathematics of Diffusion. Oxford University Press, Oxford, UK.
28. Yang, B., and A. S. Verkman. 1997. Water and glycerol permeabilities of aquaporins 1–5 and MIP determined quantitatively by expression of epitope-tagged constructs in *Xenopus* oocytes. *J. Biol. Chem.* 272: 16140–16146.
29. Beitz, E., S. Pavlovic-Djuranovic, …, J. E. Schultz. 2004. Molecular dissection of water and glycerol permeability of the aquaglyceroporin from *Plasmodium falciparum* by mutational analysis. *Proc. Natl. Acad. Sci. USA.* 101:1153–1158.
30. Karlgren, S., N. Pettersson, …, S. Hohmann. 2005. Conditional osmotic stress in yeast: a system to study transport through aquaglyceroporins and osmostress signaling. *J. Biol. Chem.* 280:7186–7193.
31. Smith, Z. J. 2009. Integrated Raman and Angular Scattering of Single Biological Cells. ProQuest, Ann Arbor, MI.
32. Lide, D. R. 1999. The CRC Handbook of Chemistry and Physics, 80th Ed. CRC Press/Taylor & Francis, Boca Raton, FL.
33. Smith, A. J., and A. S. Verkman. 2015. Superresolution imaging of aquaporin-4 cluster size in antibody-stained paraffin brain sections. *Biophys. J.* 109:2511–2522.
34. Picco, A., M. Mund, …, M. Kaksonen. 2015. Visualizing the functional architecture of the endocytic machinery. *eLife.* 4:e04535.
35. Berg, H. C. 1993. Random Walks in Biology. Princeton University Press, Princeton, NJ.
36. Grunnet, M., N. MacAulay, …, D. A. Klaerke. 2002. Regulation of cloned, Ca^{2+}-activated K^{+} channels by cell volume changes. *Pflugers Arch.* 444:167–177.
37. Mazzochi, C., J. K. Bubien, …, D. J. Benos. 2006. The carboxyl terminus of the α-subunit of the amiloride-sensitive epithelial sodium channel binds to F-actin. *J. Biol. Chem.* 281:6528–6538.
38. Zhang, Y., X. F. Zhang, …, L. K. Kaczmarek. 2016. Kv3. 3 channels bind Hax-1 and Arp2/3 to assemble a stable local actin network that regulates channel gating. *Cell.* 165:434–448.
39. Stroka, K. M., H. Jiang, …, K. Konstantopoulos. 2014. Water permeation drives tumor cell migration in confined microenvironments. *Cell.* 157:611–623.
40. Oparka, K. J., K. M. Wright, …, E. J. Allan. 1993. Fluid-phase endocytosis: do plants need it? *J. Exp. Bot.* 44:247–255.
41. Hawes, C., K. Crooks, …, B. Satiat-Jeunemaitre. 1995. Endocytosis in plants: fact or artefact? *Plant Cell Environ.* 18:1245–1252.
42. Baluška, F., A. Hlavacka, …, D. Volkmann. 2002. F-actin-dependent endocytosis of cell wall pectins in meristematic root cells. Insights from Brefeldin A-induced compartments. *Plant Physiol.* 130:422–431.
43. Baluška, F., J. Šamaj, …, D. Volkmann. 2004. Actin-dependent fluid-phase endocytosis in inner cortex cells of maize root apices. *J. Exp. Bot.* 55:463–473.
44. Sun, Y., A. C. Martin, and D. G. Drubin. 2006. Endocytic internalization in budding yeast requires coordinated actin nucleation and myosin motor activity. *Dev. Cell.* 11:33–46.
45. Yamada, A., A. Mamane, …, P. Bassereau. 2014. Catch-bond behaviour facilitates membrane tubulation by non-processive myosin 1b. *Nat. Commun.* 5:3624.
46. Greenberg, M. J., T. Lin, …, E. M. Ostap. 2012. Myosin IC generates power over a range of loads via a new tension-sensing mechanism. *Proc. Natl. Acad. Sci. USA.* 109:E2433–E2440.
47. Urbanek, A. N., A. P. Smith, …, K. R. Ayscough. 2013. A novel actin-binding motif in Las17/WASP nucleates actin filaments independently of Arp2/3. *Curr. Biol.* 23:196–203.
48. Dmitrieff, S., and F. Nédélec. 2016. Amplification of actin polymerization forces. *J. Cell Biol.* 212:763–766.